



## Article

# Solid-State Structural Transformation and Photoluminescence Properties of Supramolecular Coordination Compounds

Dipankar Ghosh , Oddný Ragnarsdóttir, Daníel Arnar Tómasson and Krishna K. Damodaran \* 

Department of Chemistry, Science Institute, University of Iceland, Dunhagi 3, 107 Reykjavík, Iceland; dig11@hi.is (D.G.); odr3@hi.is (O.R.); dat9@hi.is (D.A.T.)

\* Correspondence: krishna@hi.is; Tel.: +354-525-4846; Fax: +354-552-8911

**Abstract:** The combination of strong coordination bonds and hydrogen bonding interactions were used to generate a series of supramolecular coordination materials (SCMs), which was achieved by reacting a bis-pyridyl amide ligand, namely *N*-(4-pyridyl)nicotinamide (4PNA) with copper(II), zinc(II), and cadmium(II) benzoates. The SCMs were structurally characterized using X-ray diffraction and the key intermolecular interactions were identified via Hirshfeld surface analysis. The role of solvent molecules on the supramolecular architecture was analyzed by synthesizing the SCMs in different solvents/solvent mixtures. A solvent-mediated solid-state structural transformation was observed in copper(II) SCMs and we were able to isolate the intermediate form of the crystal-to-crystal transformation process. The luminescence experiments revealed that complexation enhanced the fluorescence properties of 4PNA in the zinc(II) and cadmium(II) SCMs, but a reverse phenomenon was observed in the copper(II) SCMs. This work demonstrated the tuning of supramolecular assembly in coordination compounds as a function of solvents for generating SCMs with diverse properties.

**Keywords:** supramolecular coordination materials; hydrogen bonding; crystal-to-crystal transformation; Hirshfeld surface analysis; photoluminescence



**Citation:** Ghosh, D.; Ragnarsdóttir, O.; Tómasson, D.A.; Damodaran, K.K. Solid-State Structural Transformation and Photoluminescence Properties of Supramolecular Coordination Compounds. *Symmetry* **2021**, *13*, 112. <https://doi.org/10.3390/sym13010112>

Received: 26 December 2020

Accepted: 6 January 2021

Published: 11 January 2021

**Publisher's Note:** MDPI stays neutral with regard to jurisdictional claims in published maps and institutional affiliations.



**Copyright:** © 2021 by the authors. Licensee MDPI, Basel, Switzerland. This article is an open access article distributed under the terms and conditions of the Creative Commons Attribution (CC BY) license (<https://creativecommons.org/licenses/by/4.0/>).

## 1. Introduction

Supramolecular coordination chemistry [1–5], which is a combination of coordination chemistry and hydrogen bonding interactions, plays an essential role in the self-assembly of biologically active metal complexes. Nature has been successful at tuning the self-assembly process of coordination complexes by exploiting hydrogen-bonding interactions to generate biologically active metal complexes [6], such as proteins and enzymes. The recent advances in supramolecular chemistry have enabled researchers to assemble hydrogen-bonded coordination compounds to complex structures with intriguing properties, such as anticancer agents [7], DNA binding [8], guest entrapment [9], inclusion compounds [10], and catalytic activity [11]. The hydrogen bonding capability of coordination complexes was proposed by Mingos and co-workers [5], which could lead to the self-assembly of these complexes into one (1-D), two (2-D), and three (3-D) dimensional supramolecular coordination materials (SCMs). SCMs can be classified into three groups, namely, metal-bound, part of a metal-bound ligand, and external to the complex, based on the relative position of the metal center and the hydrogen bonding groups [12]. However, the synthesis of a supramolecular coordination compound with desirable properties is challenging because the final supramolecular architecture depends on various parameters, such as the nature of the metal center, coordination modes of the ligands, the metal:ligand ratio, and reaction conditions, such as the temperature and solvent systems [13].

The systematic design of a SCM includes the combination of hydrogen bonding functionalities, consisting of hydrogen bond donors and acceptors or synthons involving self-complementary hydrogen bonds, and the coordinating abilities of metals and ligands [3,4,12]. The nitrogen atoms of the urea and amide moieties and oxygen atoms of hydroxy groups are excellent hydrogen bond donors. On the other hand, the acceptors

include the oxygen atoms of urea/amide, carboxylate, carboxamide moieties, and the nitrogen atoms of imidazole, pyrazole, pyridine, and pyrimidine. The hydrogen bonding groups, such as urea and amide moieties, have been extensively used to generate SCMs by utilizing the complementary  $C=O \cdots H-N$  hydrogen bonding [14–16], which may play a significant role in the internetwork supramolecular recognition process. The adjacent functional groups strongly influence the hydrogen bonding synthons; for example, attaching a pyridyl group to urea or an amide moiety could modify the intermolecular interactions [17,18]. This will result in the modification of the complementary amide hydrogen bonding to the  $N \cdots H-N$  hydrogen-bonding synthon involving the urea/amide group and the pyridyl moiety [17,18]. The supramolecular assembly via amide  $\cdots$  amide hydrogen bonds in nicotinamide-based transition metal complexes was reported by Akeroy's group [19]. Puddephatt et al. showed that the amide  $\cdots$  amide interactions enabled the formation of molecular triangles in a platinum complex of bis-pyridyl amides and a 2,2'-bipyridine derivative with an encapsulated triflate anion [20]. These results demonstrated the significance of combining coordination and hydrogen-bonding groups to generate SCMs, which resulted in a myriad of pyridyl-amide based SCMs as functional supramolecular materials [21–23] with intriguing applications in biological processes [23,24] and as catalysts [25], metallogels [26], luminescent materials [27], and sensors [28].

Although metal–ligand coordination and hydrogen bonding are the key driving forces in SCMs, various parameters, such as solvents, temperature, and anions, also play an essential role in generating the final supramolecular architecture [21–23,29–41]. Dastidar et al. reported the significance of hydrogen bonding moieties in recognizing hydrogen-bond-capable guest molecules, which was evident from the encapsulation of a  $(H_2O)_{14}$  water cluster in pyridyl amide-based coordination polymers [34]. Specifically, the effects of these interactions are prominent in the self-assembly of supramolecular complexes (SCCs) compared to the polymeric SCMs. We have shown that SCCs based on copper(II) complexes of the bis-pyridyl amide ligand, *N*-(4-pyridyl)nicotinamide (4PNA), selectively formed gel in an aqueous solution of DMF/DMSO [35]. The solvent molecules play an essential role in the formation of the metal–ligand bond [36], solvent-induced structural transformation [37–39], and polymorphism [40], and tuning the SCCs from a centrosymmetric structure to a non-centrosymmetric structure [41]. This prompted us to study the role of solvent molecules in SCCs based on 4PNA and benzoate ligands, which will enable us to evaluate the effect of hydrogen bonding motifs and solvent molecules in the supramolecular architectures.

## 2. Materials and Methods

All starting materials and solvents were purchased from Sigma-Aldrich (MEDOR ehf, Reykjavik, Iceland) and used as supplied, and deionized water was used in all experiments. The ligand, 4PNA, was synthesized as per the reported procedure [18] and the metal benzoates were synthesized by layering ethanolic metal nitrate solutions over an aqueous sodium benzoate solution.  $^1H$ -NMR (Figure S1, see Supplementary Materials) were recorded on a Bruker Avance 400 MHz spectrometer (Rheinstetten, Germany) and FT-IR spectra were obtained using Nicolet iS10 instrument (Madison, WI, US). Single-crystal X-ray diffraction (SCXRD) and X-ray powder diffraction (XRPD) analyses were performed on a Bruker D8 VENTURE (Karlsruhe, Germany) and PANalytical instrument (Almelo, The Netherlands), respectively.

### 2.1. Synthesis of SCMs

#### 2.1.1. $[Cu(PhCO_2)_2(4PNA)_2]$ (1)

A mixture of copper(II) benzoate (30.5 mg, 0.1 mmol) and 10.0 mL MeOH was heated at 60.0 °C and sonicated for a minute to obtain a saturated solution. The mixture was filtered to remove the undissolved solid material and was added to an ethanolic solution (5.0 mL) of 4PNA (40.0 mg, 0.2 mmol). Slow evaporation of the solution resulted in block-shaped purple crystals of **1** in two days. Yield: 20.0%. FT-IR (KBr,  $cm^{-1}$ ): 3258, 3177, 3074,

3015, 2963, 1686, 1598, 1558, 1507, 1477, 1446, 1428, 1418, 1389, 1332, 1295, 1262, 1206, 1173, 1103, 1062, 1023, 896, 850, 839, 801, 718, 685, 621, 600, 542.

#### 2.1.2. $\{[\text{Cu}(\text{PhCO}_2)_2(4\text{PNA})_2] \cdot x\text{H}_2\text{O}\}$ (**1.S**)

A mixture of copper(II) benzoate (30.5 mg, 0.1 mmol) and 3.5 mL DMF was heated gently at 50.0–60.0 °C and filtered to obtain a clear green solution, which was added to a 1:1 DMF/water (*v/v*) solution (1.0 mL) of 4PNA (40.0 mg, 0.2 mmol). Purple plate-shaped crystals of **1.S** were obtained via slow evaporation over three days. Yield: 18.0%. FT-IR (KBr,  $\text{cm}^{-1}$ ): 3260, 3178, 3074, 1686, 1598, 1557, 1508, 1477, 1447, 1428, 1418, 1390, 1332, 1295, 1242, 1207, 1174, 1138, 1113, 1063, 1025, 896, 850, 839, 801, 720, 686, 621, 600, 542.

#### 2.1.3. $\{[\text{Cu}(\text{PhCO}_2)_2(4\text{PNA})_2] \cdot \text{H}_2\text{O}\}_2$ (**2**)

A solution of copper(II) benzoate (30.5 mg, 0.1 mmol) in 10.0 mL DMF was layered over an aqueous solution (10.0 mL) of 4PNA (40.0 mg, 0.2 mmol). Slow evaporation of the solution resulted in blue plate-shaped crystals of **2** after 2–3 days. Yield: 40.0%. FT-IR (KBr,  $\text{cm}^{-1}$ ): 3547, 3263, 3173, 3066, 1687, 1667, 1600, 1573, 1555, 1512, 1446, 1429, 1420, 1379, 1332, 1299, 1268, 1212, 1173, 1115, 1103, 1068, 1026, 896, 838, 721, 708, 684, 597, 539.

#### 2.1.4. $\{[\text{Zn}(\text{PhCO}_2)_2(4\text{PNA})_2] \cdot \text{DMF}\}$ (**3**)

A solution of 4PNA (40.0 mg, 0.2 mmol) in 0.5 mL of DMF was added to a solution of zinc(II) benzoate (30.7 mg, 0.1 mmol) in 3.0 mL DMF and the mixture was left at room temperature for slow evaporation. The crystals of **3** were isolated as colorless needles in four days. Yield: 10.0%.  $^1\text{H-NMR}$  (400 MHz,  $\text{DMSO-}d_6$ ):  $\delta$  (ppm) = 10.80 (2H, s), 9.12 (2H, d,  $J = 2.34$ ), 8.80 (2H, dd,  $J = 4.80, 1.68$ ), 8.52 (4H, m), 8.31 (2H, dd,  $J = 8.00, 2.36$ ), 7.95 (5H, m), 7.79 (4H, m), 7.60 (2H, dd,  $J = 7.96, 4.84$ ), 7.48 (2H, m), 7.41 (4H, m), 2.89 (3H, s), 2.73 (3H, s). FT-IR (KBr,  $\text{cm}^{-1}$ ): 3265, 3170, 3074, 1695, 1600, 1558, 1528, 1517, 1500, 1447, 1431, 1393, 1335, 1312, 1274, 1214, 1175, 1126, 1104, 1064, 1055, 1022, 965, 934, 899, 848, 817, 721, 683, 649, 606, 540.

#### 2.1.5. $[\text{Zn}(\text{PhCO}_2)_2(4\text{PNA})]_n$ (**4**)

A solution of zinc(II) benzoate (30.7 mg, 0.1 mmol) in 10.0 mL MeOH was layered over an ethanolic solution (5.0 mL) of 4PNA (40.0 mg, 0.2 mmol). The slow evaporation of the above solution resulted in block-shaped colorless crystals of **4** in two days. Yield: 60.0%.  $^1\text{H-NMR}$  (400 MHz,  $\text{DMSO-}d_6$ ):  $\delta$  (ppm) = 10.85 (1H, s), 9.12 (1H, d,  $J = 2.40$ ), 8.80 (1H, dd,  $J = 4.84, 1.68$ ), 8.54 (2H, m), 8.31 (1H, dd,  $J = 7.68, 0.64$ ), 7.96 (4H, m), 7.82 (2H, m), 7.61 (1H, dd,  $J = 4.80, 2.24$ ), 7.49 (2H, m), 7.41 (4H, m). FT-IR (KBr,  $\text{cm}^{-1}$ ): 3434, 3265, 3170, 3074, 1695, 1600, 1558, 1528, 1517, 1500, 1447, 1431, 1392, 1335, 1312, 1275, 1214, 1175, 1126, 1104, 1064, 1055, 1022, 899, 848, 721, 688, 650, 606, 540.

#### 2.1.6. $\{[\text{Cd}(\text{PhCO}_2)_2(4\text{PNA})_2] \cdot \text{DMF}\}_2$ (**5**)

A mixture of 4PNA (40.0 mg, 0.2 mmol) and cadmium(II) benzoate (35.5 mg, 0.1 mmol) was dissolved in 3.0 mL DMF and left at room temperature. Slow evaporation of the solution resulted in colorless rod-shaped crystals of **5**. Yield: 50.0  $^1\text{H-NMR}$  (400 MHz,  $\text{DMSO-}d_6$ ):  $\delta$  (ppm) = 10.78 (2H, s), 9.12 (2H, m), 8.80 (2H, dd,  $J = 4.84, 1.72$ ), 8.51 (4H, m), 8.31 (2H, dd,  $J = 7.92, 2.32$ ), 7.97 (5H, m), 7.78 (4H, m), 7.60 (2H, dd,  $J = 8.00, 4.84$ ), 7.47 (2H, m), 7.41 (4H, m), 2.89 (3H, s), 2.73 (3H, s). FT-IR (KBr,  $\text{cm}^{-1}$ ): 3259, 3178, 3062, 1689, 1658, 1595, 1542, 1522, 1421, 1401, 1332, 1301, 1277, 1213, 1116, 1100, 1066, 1024, 1014, 895, 851, 832, 725, 713, 682, 663, 621, 590, 534.

#### 2.1.7. $[\text{Cd}(\text{PhCO}_2)_2(4\text{PNA})]_n$ (**6**)

The polymer **6** was synthesized following a similar procedure to that used for compound **4** by layering a cadmium(II) benzoate (35.5 mg, 0.1 mmol) solution in MeOH (10.0 mL) over an ethanolic solution (5.0 mL) of 4PNA (40.0 mg, 0.2 mmol) and left to undergo slow evaporation. Colorless plate-shaped crystals of **6** were obtained in three

days. Yield: 55.0%.  $^1\text{H-NMR}$  (400 MHz,  $\text{DMSO-}d_6$ ):  $\delta$  (ppm) = 10.79 (1H, s), 9.12 (1H, d,  $J = 2.32$ ), 8.80 (1H, dd,  $J = 4.76, 1.68$ ), 8.51 (2H, m), 8.31 (1H, dt,  $J = 6.00, 1.96$ ), 7.96 (4H, m), 7.78 (2H, m), 7.60 (1H, dd,  $J = 8.00, 4.84$ ), 7.47 (2H, m), 7.41 (4H, m). FT-IR (KBr,  $\text{cm}^{-1}$ ): 3263, 3180, 3090, 3069, 1697, 1595, 1523, 1496, 1445, 1401, 1332, 1308, 1274, 1214, 1194, 1176, 1123, 1069, 1051, 1026, 1014, 963, 893, 843, 721, 683, 644, 601, 540.

## 2.2. Crystal-to-Crystal Transformation

### 2.2.1. Transformation of **1** to **2**

The crystals of **1** ( $\approx 2.0$  mg) were transferred into a vial and 5.0 mL of the solvent (water or MeOH/water or EtOH/water or DMF/water) was added to it. The color of the material slowly changed from purple to blue and plate-shaped crystals of **2** were obtained in four days. The conversion of **1** to **2** was confirmed by analyzing the unit cell parameters using SCXRD and comparing the XRPD data.

### 2.2.2. Transformation of **1.S** to **2**

The crystals of the complex **1.S** were left in the mother liquor for four days. The purple crystals of **1.S** were gradually converted to blue complex **2**, which was confirmed using SCXRD and XRPD data. The isolated crystals of **1.S** that were immersed in 5.0 mL of the solvent (water or MeOH/water or EtOH/water or DMF/water) also transformed into **2**.

### 2.2.3. Transformation of **1.S** to **1**

The crystals of **1.S** were air-dried under a fume hood for four days, and the XRPD analysis was performed on the dried crystals. The XRPD pattern of the dried crystals matched with the bulk crystals of **1**.

## 2.3. Single-Crystal X-ray Diffraction

We have performed single crystal X-ray analysis on a Bruker D8 VENTURE (Photon100 CMOS detector) diffractometer, which was connected to a low temperature device, namely Cryostream open-flow nitrogen cryostat. The crystals of 4PNA complexes/polymers suitable for SCXRD were isolated and coated with cryogenic oil before mounting. The data were collected using  $\text{MoK}\alpha$  ( $\lambda = 0.71073 \text{ \AA}$ ) or  $\text{CuK}\alpha$  ( $\lambda = 1.54178 \text{ \AA}$ ) radiation. We used Apex III (Bruker AXS, Madison, WI, USA) for determining unit cell, collecting the diffraction pattern, for absorption correction and solving/refining the data to a proper model. We used the direct method, and the data was refined using SHELXTL [42], version 2017/1. All non-disordered non-hydrogen atoms were refined anisotropically, except the disordered oxygen atom of the benzoate anion in **5**, which was refined using free variable (FVAR) instruction. The position of the hydrogen atoms were fixed, and the riding model was used to refine the fixed positions, except for complex **2**, where the peaks connected to the oxygen atoms on the Fourier map were assigned as hydrogen atoms and refined. We could not find a proper model for the disordered solvent molecules in **1.S**, and the contribution of the electron densities from the solvent molecules was excluded from the refinement using PLATON/SQUEEZE [43]. The crystallographic data for the complexes reported herein have been deposited at the Cambridge Crystallographic Data Centre, and the CCDC numbers are 2052228–2052234. These data can be obtained free of charge via [www.ccdc.cam.ac.uk/data\\_request/cif](http://www.ccdc.cam.ac.uk/data_request/cif), or by emailing [data\\_request@ccdc.cam.ac.uk](mailto:data_request@ccdc.cam.ac.uk).

## 2.4. X-ray Powder Diffraction

The crystals of the complexes/polymers were dried in a fume hood to remove any residual solvent and were ground into a fine powder. The samples were prepared by making a thin layer of the finely powdered sample ( $\approx 10.0$  mg) on a glass slide. XRPD was carried out on a PANalytical instrument ( $\text{CuK}\alpha$  radiation,  $\lambda = 1.54178 \text{ \AA}$ ) in the  $2\theta$  range of  $4.0\text{--}60.0^\circ$  using a  $0.02^\circ$  step size.

### 2.5. Luminescence

The UV-absorption experiment ( $10^{-4}$  M in MeCN) was carried out on a PerkinElmer Lambda 25 UV/Vis Spectrometer (Shelton, CT, USA) and the fluorescence experiments ( $10^{-3}$  M in MeCN) were performed on a FluoroMax-4 spectrofluorometer instrument (Edison, NJ, USA) at 20.0 °C. The corresponding compound (0.01 mmol) was dissolved in 10.0 mL MeCN by heating and sonicating, and cooled to room temperature to obtain a  $10^{-3}$  M solution. The solution was excited at 295 nm and the emission spectrum was collected at intervals of 1 nm from 300–720 nm with a slit width of 5 nm.

## 3. Results

### 3.1. Structural Analysis

The reaction of 4PNA with the corresponding metal benzoate yielded supramolecular complexes and these complexes were characterized using single-crystal X-ray diffraction analysis. The crystallographic data and hydrogen bonding parameters are given in Tables S1 and S2 (see Supplementary Materials), respectively.

#### 3.1.1. Structural Analysis of **1** and **1.S**

Single-crystal X-ray analysis of the crystals obtained by layering an ethanolic solution of 4PNA over copper(II) benzoate in methanol revealed the formation of SCC (**1**) with a formula of  $[\text{Cu}(\text{PhCO}_2)_2(4\text{PNA})_2]$ . The copper(II) metal center lay on an inversion center and displayed a distorted octahedral geometry. The equatorial positions of the metal center were occupied by two benzoate ligands that were coordinated to the metal center in an asymmetric chelate coordination mode. The pyridyl nitrogen atom of the aminopyridine end of the 4PNA molecules was coordinated to the axial positions. In contrast, the pyridyl nitrogen atom of the nicotinoyl end was found to be non-coordinated (Figure 1a). The oxygen atom of the metal-bound carboxylate was hydrogen-bonded to the amide moiety of 4PNA, resulting in a 1-D hydrogen-bonded chain ( $\text{N} \cdots \text{O} = 2.8188(19) \text{ \AA}$ ). The adjacent 1-D chains interacted via  $\text{C-H} \cdots \text{O}$  and  $\text{C-H} \cdots \text{N}$  interactions to form the 3-D hydrogen-bonded architecture (Figure S2, see Supplementary Materials). Analysis of the crystals obtained by changing the solvent system revealed the formation of an inclusion compound (**1.S**) with a formula of  $\{[\text{Cu}(\text{PhCO}_2)_2(4\text{PNA})_2] \cdot x\text{H}_2\text{O}\}$  and the complex was found to be isostructural with **1** (Figure S3, see Supplementary Materials). XRPD analysis of the air-dried crystals of **1.S** (four days) revealed the conversion of **1.S** to **1** via a crystal-to-crystal transformation. The crystals of **1** or **1.S** were immersed in water or aqueous solvents, such as MeOH/water, EtOH/water, and DMF/water, and the SCXRD analysis performed on these crystals after three days revealed a crystal-to-crystal transformation that resulted in a complex with a formula of  $\{[\text{Cu}(\text{PhCO}_2)_2(4\text{PNA})_2] \cdot \text{H}_2\text{O}\}_2$  (**2**).

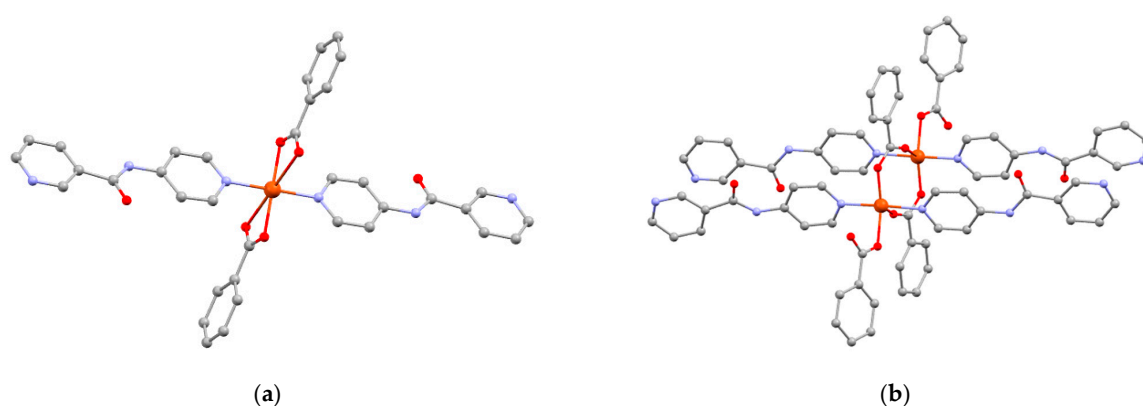


**Figure 1.** Molecular structure of **1** and **2**: (a) the distorted octahedral geometry of Cu(II) in **1**; (b) the dinuclear complex displaying distorted trigonal bipyramidal geometry in **2** (the hydrogen atoms are omitted for clarity).

### 3.1.2. Structural Analysis of 2

The crystallization experiments using copper(II) benzoate and 4PNA that were performed by increasing the amount of water in the DMF/water mixture also resulted in plate-shaped blue crystals of complex **2**. The structural analysis of the crystals revealed the formation of a dinuclear complex, and the Cu(II) centers were bridged by two benzoate ligands, resulting in a dinuclear metallo-macrocycle (Figure 1b). The metal center displayed distorted trigonal bipyramidal geometry, with the pyridyl nitrogen atoms of the aminopyridine end of four 4PNA molecules occupying the axial positions of two copper(II) metal centers. The solvent water molecule was hydrogen-bonded to the amide moieties of adjacent 4PNA molecules, which was stabilized by the N–H...O and O–H...O interactions (Figure S2, see Supplementary Materials). These water molecules interacted with the pyridyl nitrogen atoms of the adjacent metallo-macrocycle via O–H...N interactions to form a 1-D hydrogen-bonded chain. The 1-D chains interacted via N–H...O interactions involving the amide moiety of one of the 4PNA molecules and the carbonyl oxygen atom of the benzoate, resulting in a 2-D hydrogen-bonded network.

### 3.1.3. Structural Analysis of 3

Single-crystal X-ray analysis of the colorless crystals obtained via the slow evaporation of a solution of 4PNA and zinc(II) benzoate in DMF confirmed the formation of complex **3**  $[\text{Zn}(\text{PhCO}_2)_2(4\text{PNA})_2]\cdot\text{DMF}$ . The Zn(II) metal center displayed a tetrahedral geometry with two benzoate ions that were coordinated in a monodentate fashion and two 4PNA molecules coordinated via pyridyl nitrogen of the aminopyridine end (Figure 2a). The amide moieties were hydrogen-bonded to the oxygen atom of the benzoate ion (Figure S4, see Supplementary Materials), resulting in a 1-D hydrogen-bonded chain. The non-coordinated pyridyl moiety of the nicotinoyl end of 4PNA and the solvent DMF molecule did not show hydrogen-bonding interactions but displayed weak intermolecular non-bonding interactions.

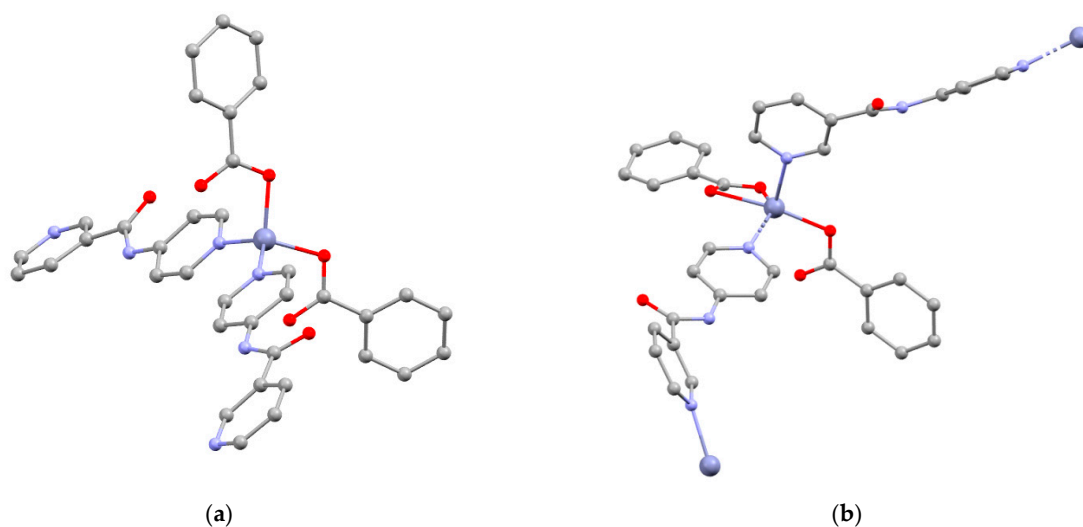


**Figure 2.** Coordination geometry of the Zn(II) metal center in (a) coordination complex **3** with a distorted trigonal bipyramidal geometry and (b) coordination polymer **4** with a distorted square pyramidal geometry (the hydrogen atoms are omitted for clarity).

### 3.1.4. Structural Analysis of 4

The reaction of 4PNA and zinc(II) benzoate was repeated in DMF/water and MeOH/EtOH, which resulted in block-shaped crystals. The structural analysis of these crystals revealed the formation of a polymeric network (**4**) with a formula of  $[\text{Zn}(\text{PhCO}_2)_2(4\text{PNA})]_n$ . One of the benzoate moieties was coordinated to the metal center in a monodentate fashion, whereas the second benzoate ion adopted an asymmetric chelate coordination mode



(Figure 2b). The 4PNA molecules interconnected the zinc(II) benzoate moieties to form a 1-D coordination polymer (Figure S5, see Supplementary Materials). The Zn(II) metal center's geometry can be considered a distorted square pyramidal geometry. The amide moiety of the 1-D polymeric chains displayed a hydrogen-bonding interaction with the carbonyl oxygen atom of the monodentate benzoate ion of the adjacent chains to form a 2-D hydrogen-bonded network (Figure S4, see Supplementary Materials).

### 3.1.5. Structural Analysis of 5

The reaction of cadmium(II) benzoate and 4PNA in DMF at room temperature yielded X-ray-quality crystals, and the structural analysis revealed the formation of the dinuclear complex **5** with a formula of  $[\text{Cd}(\text{PhCO}_2)_2(4\text{PNA})_2]\cdot\text{DMF}_2$ . The equatorial positions of the Cd(II) metal center were occupied by the oxygen atoms of the benzoate ions and the pyridyl moiety of the aminopyridine end of 4PNA was coordinated to the axial position to form an octahedral Cd(II) metal center. However, the oxygen atoms of one of the benzoates displayed a bidentate coordination mode with the Cd(II) center of the adjacent molecule to form a metallo-macrocycle with a distorted pentagonal bipyramidal geometry (Figure 3a). The pyridyl moiety of the nicotinoyl end of 4PNA and the solvent DMF molecules were found to be non-coordinated, similar to **3**, but the amide moiety of one of the 4PNA molecules displayed hydrogen bonding with the oxygen atoms of the DMF molecule (Figure S6, see Supplementary Materials). The metallo-macrocycles were interconnected via a hydrogen-bonding interaction between the amide moieties of the other 4PNA and the oxygen atom of the benzoate ion, resulting in a 1-D hydrogen-bonded macrocyclic chain.

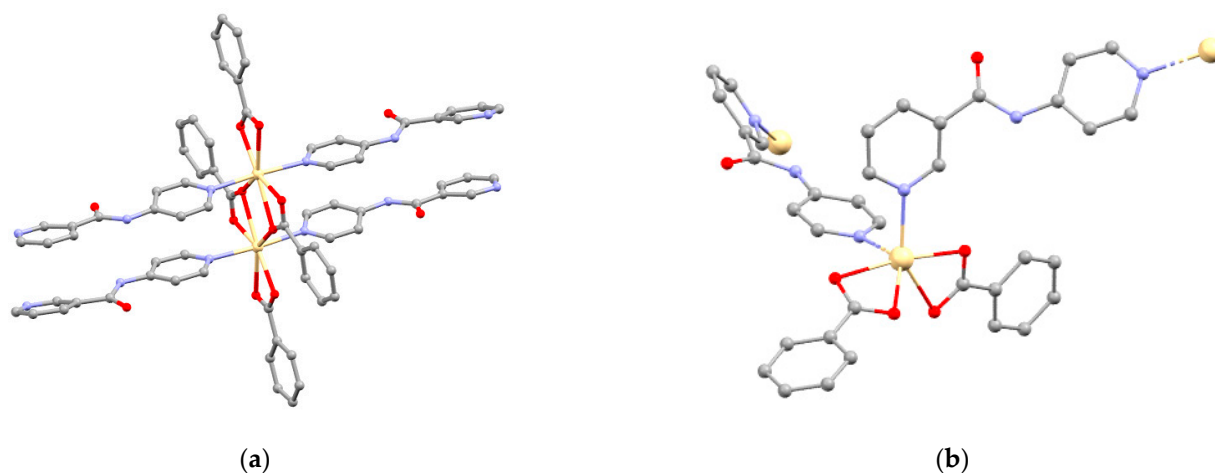


**Figure 3.** Coordination geometry of the cadmium(II) supramolecular coordination materials (SCMs): (a) a metallo-macrocycle with Cd(II) displaying distorted pentagonal bipyramidal geometry and (b) a *cis*-coordination of 4PNA, resulting in coordination polymer **6** (the hydrogen atoms are omitted for clarity).

### 3.1.6. Structural Analysis of 6

The X-ray analysis of the plate-shaped crystal obtained by layering a solution of cadmium(II) benzoate (methanol or DMF) over a solution of 4PNA (ethanol or water) revealed that a coordination polymer (**6**) with a formula of  $[\text{Cd}(\text{PhCO}_2)_2(4\text{PNA})]_n$  was formed (Figure 3b). In the crystal structure, the benzoate ions displayed bidentate coordination modes with the metal centers interconnected by 4PNA molecules to form a 1-D coordination polymer (Figure S5, see Supplementary Materials) similar to **4**. Although the coordination mode of 4PNA was identical to **4**, the coordination geometry of the Cd(II) metal center in **6** could be assigned as a distorted trigonal anti-prismatic geometry. The non-bonding interactions were similar to the zinc(II) coordination polymer (Figure S6, see Supplementary Materials).

### 3.2. X-ray Powder Diffraction

The phase purity of the SCMs was confirmed by comparing the XRPD pattern of the crystals and the simulated pattern calculated from the crystal structure. The bulk crystals were filtered from the mother liquor, air-dried, and ground into a fine powder for XRPD analysis. The XRPD pattern of the complexes synthesized in bulk scale matched with the simulated pattern obtained from the SCXRD data (Figure 4 and Figures S7–S11, see Supplementary Materials). XRPD analysis was also performed on the materials obtained via the crystal-to-crystal transformation of **1** and **1.S**. The XRPD pattern of the blue crystals obtained from the solvent-mediated crystal-to-crystal transformations of **1** and **1.S** were virtually superimposable onto the pattern of complex **2** (Figure 4), and the pattern of air-dried **1.S** was similar to complex **1** (Figure S7, see Supplementary Materials).

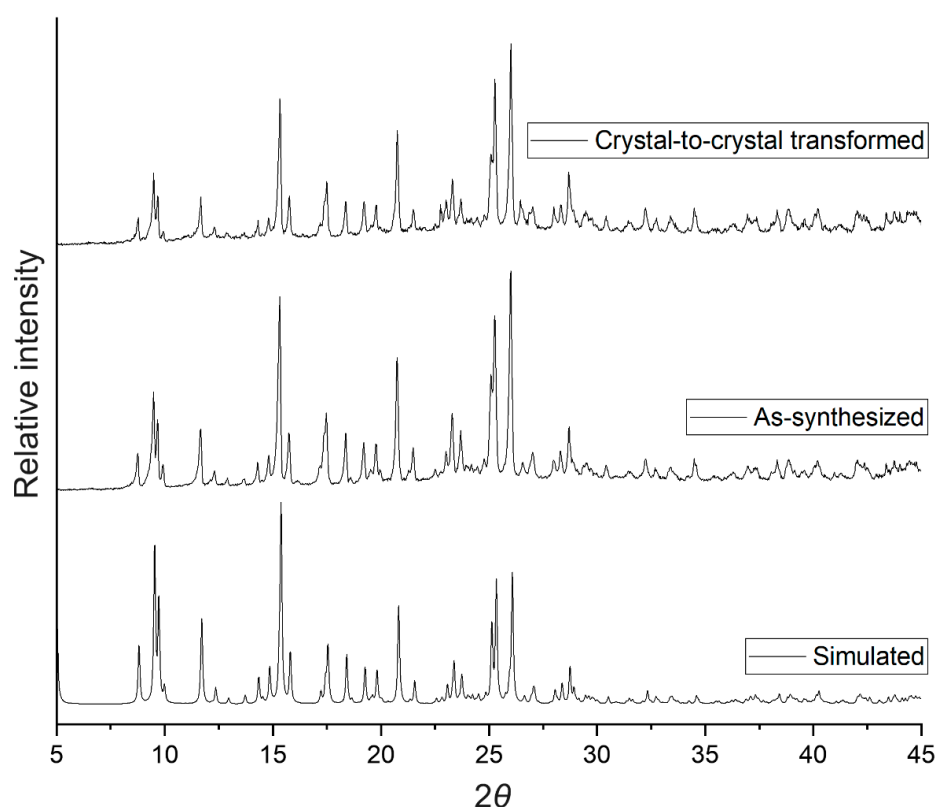


**Figure 4.** Comparison of the XRPD pattern of **2**: crystal-to-crystal transformed, as-synthesized, and simulated.

### 3.3. Hirshfeld Surface Analysis

The Hirshfeld surface was generated on a complete fragment using CrystalExplorer17 [44] following similar reports [45]; the  $d_{norm}$  maps calculated for **1** and **2** are shown in Figure 5, where the red spots of different intensities indicate various close contacts. In complex **1**, intense red spots were observed near the carboxylate and amide moieties, and relatively faint spots were observed near the nicotinoyl nitrogen atoms. In comparison, strong red spots were observed on the carboxylate, the amide, and the nicotinoyl moieties of complex **2**. The  $d_{norm}$  maps of the SCMs **3–6** (Figure 6) and **1.S** (Figure S12, see Supplementary Materials) were also plotted in a similar way.



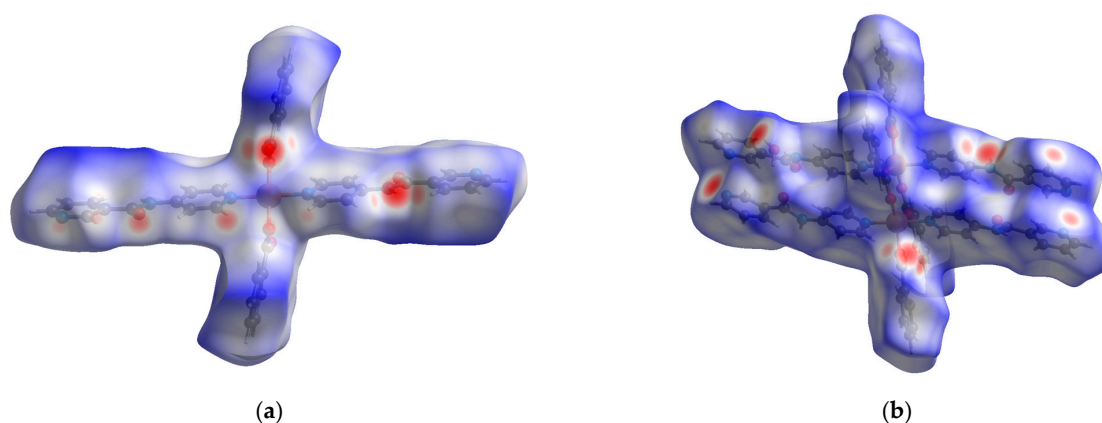


**Figure 5.** Hirshfeld surface analysis of (a) **1** and (b) **2** plotted on the  $d_{norm}$  maps displaying close contacts indicated by the red spots of varying intensities.

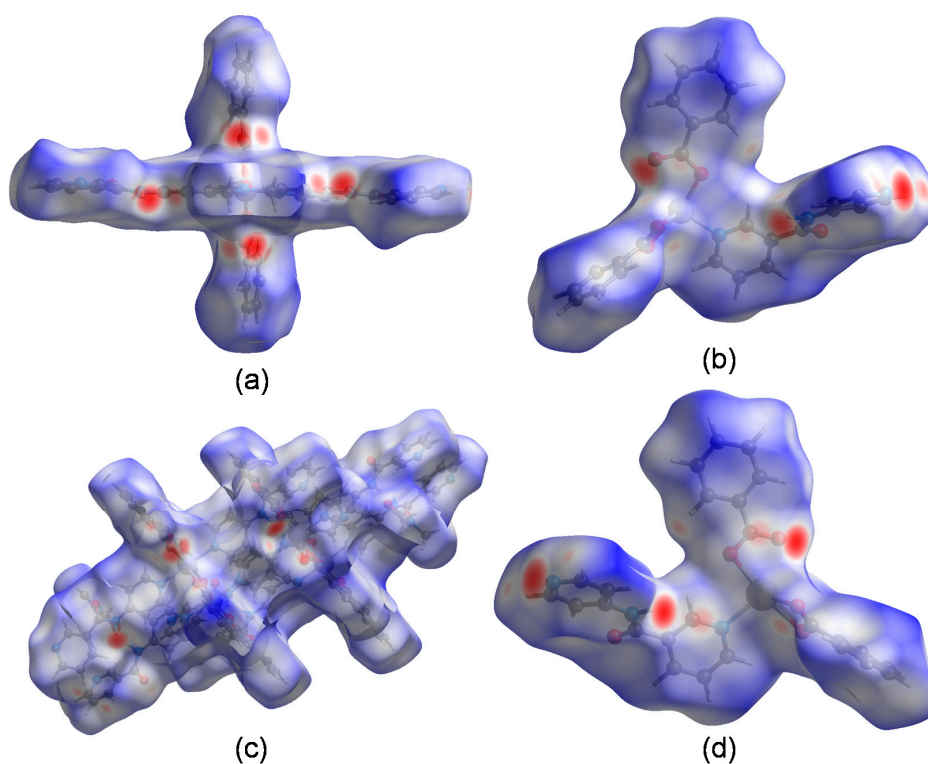


**Figure 6.** Hirshfeld surface analysis of (a) **3**, (b) **4**, (c) **5**, and (d) **6** plotted on  $d_{norm}$  maps displaying the close contacts, as indicated by the red spots of varying intensities.

In order to compare the contribution of various non-bonding interactions in the self-assembled supramolecular structure, 2-D fingerprint analysis was carried out to quantify the close contacts with neighboring hydrogen atoms. The fingerprint diagrams obtained by plotting the normalized distances of the Hirshfeld surfaces from the nearest outside and inside atoms ( $d_e$  and  $d_i$ , respectively) displayed a paw-like map for all complexes (Figure S13, see Supplementary Materials). The  $H\cdots C/C\cdots H$  interactions exhibited the highest contribution in all complexes, whereas  $H\cdots O/O\cdots H$  and  $H\cdots N/N\cdots H$  were observed on the minimum  $d_i + d_e$  contact distances. The Hirshfeld surfaces' corresponding specific non-bonding interactions were also generated (Figure S14, see Supplementary Materials).

### 3.4. Luminescence

The UV-vis absorption spectra (Figure S15, see Supplementary Materials) and the emission spectra of the metal benzoates, 4PNA ligand, and the SCMs 1–6 were recorded in MeCN at room temperature (20.0 °C). Fluorescence emission was observed for all compounds upon excitation at 295 nm (Figure 7).

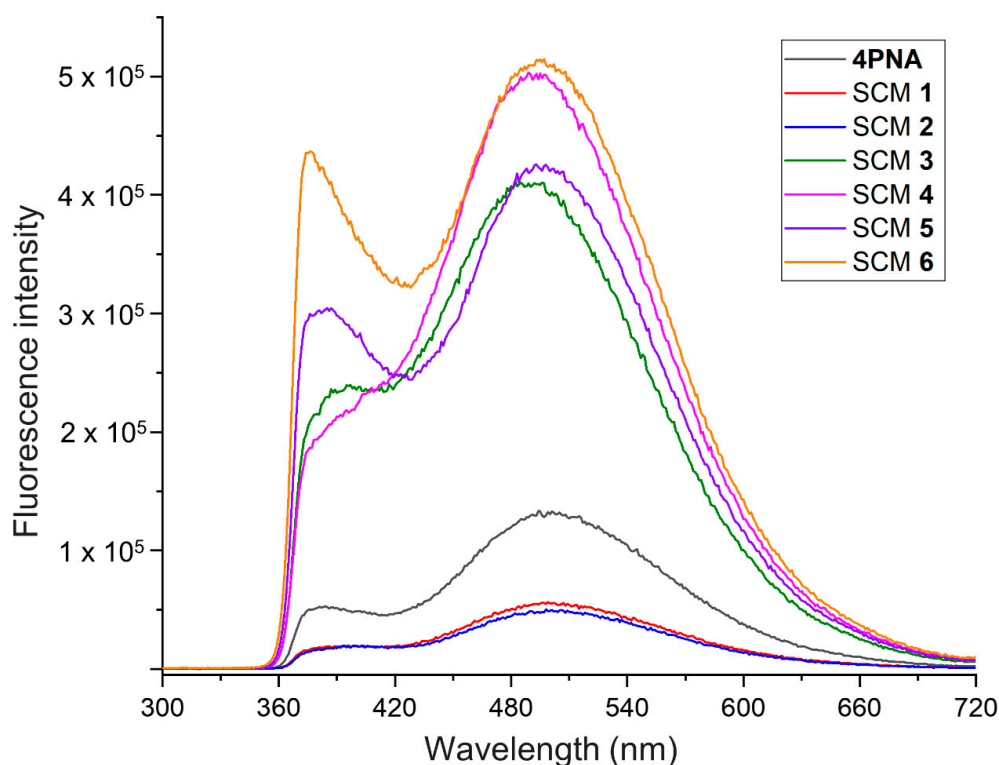


**Figure 7.** Emission spectra of the 4PNA ligand and SCMs 1–6 at room temperature in MeCN ( $\lambda_{\text{ex}} = 295$  nm).

SCMs 1–6 displayed emission bands in the range of 360–600 nm, which was similar to the free ligand 4PNA. However, there was a distinct difference in the intensities of the emission bands for the copper(II) complexes 1 and 2, which had a reduced intensity (2.5-fold for the peak at 500 nm). In contrast, the peak intensities increased from four- to five-fold for the zinc(II) and cadmium(II) SCMs (3–6). Interestingly, both the coordination polymers 4 and 6 displayed higher intensities compared to the coordination complexes 3 and 5. The emission spectra of the metal benzoates were different from the SCMs (Figure S16, see Supplementary Materials).

## 4. Discussion

The structural characterization of supramolecular complexes of metal benzoates (copper(II), zinc(II), and cadmium(II)) and hydrogen-bond-functionalized bis-pyridyl amide ligand (4PNA) was performed using SCXRD. The effect of the solvents on the supramolecular architecture was studied by crystallizing these SCMs in different solvents/solvent mixtures.

### 4.1. Solid-State Structural Analysis

The crystals obtained using the reaction of copper(II) benzoate and 4PNA in various solvent mixtures were analyzed to evaluate the role of solvent molecules on the supramolecular architecture in SCMs. The reaction in the MeOH/EtOH mixture yielded purple-colored crystals of complex 1 and the blue crystals obtained from DMF/water mixture (1:1, *v/v*) turned out to be a dinuclear complex (2). The experiment performed by varying the amount of water in the DMF/water mixture (8:1, *v/v*) resulted in an inclu-

sion compound (**1.S**). The structural analysis of **1.S** revealed the presence of disordered guest molecules and the supramolecular architecture of **1** remained intact in **1.S**; however, the solvent-accessible area per unit cell of **1** (9.5%) was expanded to 16.2% in **1.S**. The disordered solvent molecule was not involved in the hydrogen bonding interaction with the complex and the inclusion of the solvent molecule did not affect the intermolecular hydrogen bonding, which was removed using PLATON/SQUEEZE [43].

The presence of voids in the single-crystal X-ray structure of **1** prompted us to evaluate the inclusion properties of **1**, which was achieved by immersing the purple crystals in, water, MeOH/water, EtOH/water or DMF/water. After three days, blue crystals were observed in the solutions, and the structural analysis of the crystals indicated that **1** was transformed into **2** via a crystal-to-crystal transformation (Figure 8). Crystal-to-crystal transformation [46–48] can be considered as one of the best methods to unravel the solid-state self-assembly process of SCMs. The solid-state transformation via crystal-to-crystal transformation will enable us to monitor the structural change during self-assembly and often lead to products that are not accessible via routine synthetic routes [49,50]. We repeated the experiments to study the structural transformation of the inclusion compound **1.S**, which was performed by treating the crystals of **1.S** in water, MeOH/water, EtOH/water, and DMF/water. The analysis of the crystals isolated from these solutions indicated that **1.S** was transformed to **2** via crystal-to-crystal transformation (Figure 8). The reversible nature of this transformation was studied by evacuating the crystals of **1.S** and **2** at 60.0 °C for 24 h, and the structural transformation was analyzed using X-ray diffraction. A crystal-to-crystal transformation was observed for **1.S**, which was converted to **1**, but compound **2** remained unchanged. The structural transformation of **1.S** was due to the removal of the solvent molecule, which resulted in the conversion of the monoclinic space group to a triclinic space group. Thus, **1.S** can be considered as an intermediate form in the transformation of **1** to **2**.

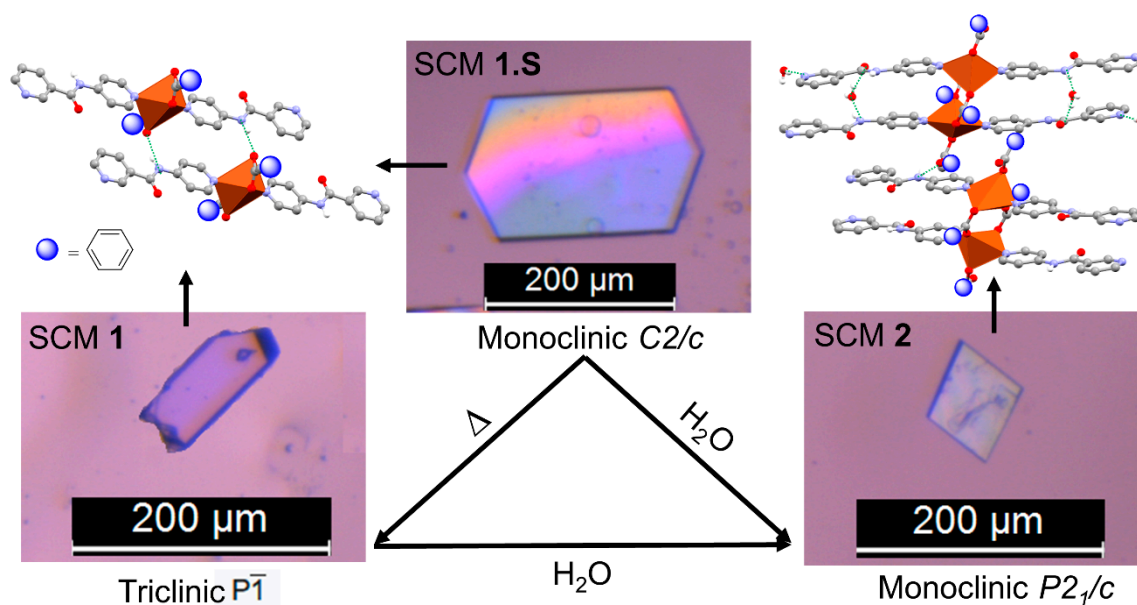


**Figure 8.** Crystal-to-crystal transformation that was observed in the Cu(II) complexes, namely, mononuclear complex **1** and **1.S** (top-left) and dinuclear complex **2** (top-right), where a dotted green line indicates hydrogen bonding.

The effect of solvent molecules was analyzed by comparing the crystal structures of **1** and **2**, which were obtained from MeOH/EtOH and DMF/water mixtures, respectively. The coordination geometry of the Cu(II) metal center in **1** was a distorted octahedral geometry, and in the case of **2**, a distorted pentagonal bipyramidal geometry was observed. One of the benzoate ions showed a bifurcated coordination bond with two metal centers in **2**, resulting in a dinuclear complex. Although the solvent molecules were not interacting

with the framework in complex **1.S**, a strong interaction was observed in **2**, and the solvent water molecule was hydrogen-bonded to the amide moieties, which was stabilized by the N—H...O and O—H...O interactions.

The crystal structure of the zinc(II) complex **3** from DMF was compared with the SCM **4** obtained from DMF/water or MeOH/EtOH mixtures to analyze the effect of solvents in the supramolecular architecture of Zn(II) complexes. The amide moieties were hydrogen-bonded to the carboxylate moieties in both cases but the coordination geometry of the Zn(II) metal center was different. The metal center of **3** displayed a tetrahedral geometry, but a distorted square pyramidal geometry was observed in **4**. Furthermore, changing the solvents induced the coordination of the two pyridyl groups in 4PNA, resulting in the formation of the coordination polymer (**4**). We analyzed the structures of the cadmium complexes obtained from different solvent/solvent mixtures. The crystallization of cadmium(II) benzoate and 4PNA in DMF resulted in a dinuclear complex (**5**), but a coordination polymer (**6**) was obtained by changing the solvent to MeOH/EtOH or DMF/water mixtures. The coordination geometries of the Cd(II) metal center were different in these structures, where a distorted pentagonal bipyramidal geometry and a distorted trigonal anti-prismatic geometry was observed in **5** and **6**, respectively. The dinuclear complex (**5**) was formed due to the bifurcated coordination mode of the oxygen atom of one of the benzoate ions, similar to complex **2**. Although the coordinated organic components of **5** were similar to those of **2**, the oxygen atoms of one of the benzoate anions in **5** displayed bidentate coordination modes. This resulted in a different coordination geometry in **5**, which was converted to a distorted pentagonal bipyramidal geometry. The non-bonding interactions and the coordination mode of 4PNA in **6** were similar to **4**, resulting in a 1-D coordination polymer. These results indicate the importance of the solvent in supramolecular coordination compounds, which had a prominent effect in dictating the final supramolecular architecture.

#### 4.2. X-ray Powder Diffraction

The XRPD pattern of the as-synthesized SCMs **1–6** was similar to the simulated pattern obtained from the single-crystal structure (Figure 4 and Figures S7–S11, see Supplementary Materials), which confirmed the phase purity of the synthesized complexes. The XRPD of the solvated complex **1.S** displayed a match with the non-solvated **1**, indicating the loss of solvent molecules during the drying process. The XRPD of complex **2** obtained via the crystal-to-crystal transformation of **1** also matched perfectly with the simulated pattern (Figure 4), revealing the complete transformation of complex **1** to **2** in the presence of water. The XRPD pattern of **2** was unchanged after heating the crystals overnight at 60.0 °C in a vacuum, indicating that form **2** is thermodynamically stable, in contrast with **1** and **1.S**.

#### 4.3. Hirshfeld Surface Analysis

The non-bonding interactions play an important role in the self-assembly process of SCMs and the analysis of different intermolecular interactions enable chemists to elucidate structure–property relationships using the crystal engineering approach [51]. The specific atom-to-atom contacts in the solid state of the SCMs were identified from the respective crystal structures, which was further extended to visualize the residue-to-residue interactions by utilizing a Hirshfeld surface analysis [44]. The Hirshfeld surface analysis was performed to study the intermolecular aggregation of the SCMs, where various red spots on the  $d_{norm}$  maps indicated the close contact and possible non-bonding interactions. The bright red spots on the carboxylate and amide moiety of **1** indicated the role of these functionalities in intermolecular interactions. The Hirshfeld surface of **2** displayed additional red spots near the nicotinoyl moiety and the water molecule, which suggested that the supramolecular assembly was dictated by nicotinoyl nitrogen and the water molecule. The intense red spot on the water molecule revealed the enhanced interactions, resulting in favorable packing within the crystal, which could explain the stability of complex **2** at 60.0 °C under a high vacuum. In the Hirshfeld surface of complex **3**, the red spots observed near the amide and carboxylate moiety were similar to **1**, indicating that the



complex was self-assembled via amide–carboxylate interactions (Figure 6). The acute red spot on the surface of **4** near the pyridyl nitrogen was due to the strong coordination bond between the metal ion and the ligand, and the other red spots with lower intensities indicated additional non-bonding interactions. The Hirshfeld surface of **5** revealed that the metallo-macrocycles were interacting via amide···carboxylate (N–H···O) interactions. The coordination polymer **6** was isostructural with **4** and the Hirshfeld surfaces of both the coordination polymers were similar.

The relative contributions of the various non-bonding interactions were quantified via the 2-D fingerprint analysis (Figure S13, see Supplementary Materials). As expected, the H···C/C···H interactions were found to be the most abundant (between 20.3–27.8%) due to the higher number of carbon atoms in the complex. The H···O/O···H interactions were significantly prominent (22.0–22.3%) in the coordination polymers **4** and **6**, where both the carboxylate and amide oxygens played a vital role in the molecular assembly. The contribution of H···O/O···H interactions was moderate (13.5–16.8%) in complex **1–3**, and low (9.3%) in complex **5** due to the low involvement of amide and carboxylate oxygens in the non-bonding interactions. The 7.0–9.7% contributions of H···N/N···H interactions in complexes **1–3** and **5** were predominately from the nicotinoyl nitrogen, and the amount was low (3.1%) in the coordination polymers **4** and **6** because both the nitrogen atoms were coordinated to the metal center.

The  $d_i + d_e$  value at any point of the fingerprint plot indicates the donor–acceptor contact distances, where a lower  $d_i + d_e$  value represents stronger intermolecular interactions. The H···O/O···H contacts exhibited the minimum  $d_i + d_e$  value in all fingerprint plots (Figure S13, see Supplementary Materials), typically  $<2.5$  Å, which fell within the hydrogen bond length. Thus, the oxygen atom acted as hydrogen bond acceptor in all the complexes, and in complex **2**, both oxygen and nitrogen atoms were involved in hydrogen bonding.

#### 4.4. Luminescence

The transition metal complexes of bis-pyridyl ligands exhibited excellent luminescence properties in both solid and solution states [52,53]. Specifically, the  $d^{10}$  metal complexes [54] and coordination polymers [55] are well-known active fluorescence probes [56], which have been utilized in the fluorescent detection of zinc(II) ions in biological systems [57], electroluminescent materials in organic light-emitting diodes (OLEDs) [58], cell imaging [59], and chemosensors [60]. The free ligand 4PNA showed blue luminescence with two bands centered at 380 and 500 nm, which may be attributed to the  $\pi^* \rightarrow \pi$  transition emission. The fluorescence experiments were performed at a higher concentration ( $10^{-3}$  M) due to the low luminescence of 4PNA. The comparison between the emission bands of metal benzoate, 4PNA, and the SCMs **1–6** clearly suggested that the fluorescence properties of the complexes were ligand-based. The emission spectra of the transition metal complexes depend on several factors, such as electron transfer,  $d-d$  transitions, and metal–ligand/ligand–metal charge transfer. The deactivation of the metal-based absorption in the visible–near IR region of Cu(II) complexes via ultrafast non-radiative pathways [53] results in poor luminescence properties. The 4PNA fluorescence intensity was quenched in complexes **1** and **2**, which may be attributed to the quenching of the fluorescence emission of the organic moieties due to the paramagnetic nature of copper(II) ions [61].

The zinc(II) and cadmium(II) ions possess a stable oxidation state and closed  $d^{10}$  electronic configuration; thus, electron transfer or  $d-d$  transitions are not expected in SCMs **3–6**. Furthermore, the fluorescence spectra were similar to the 4PNA ligand with varying intensities, which could be attributed to the intraligand  $\pi^* \rightarrow \pi$  or  $n \rightarrow \pi$  transitions [62]. The enhanced fluorescence intensity was presumably due to the introduction of a metal–ligand coordination bond, which increased the structural rigidity of 4PNA and reduced the energy loss by radiationless decay in the intraligand emission [62,63]. This was further supported by the fact that when 4PNA was coordinated at both ends to form coordination polymers **4** and **6**, the highest luminescence intensity was observed.

## 5. Conclusions

In summary, a series of supramolecular coordination complexes and coordination polymers were synthesized by reacting copper(II)/zinc(II)/cadmium(II) benzoates with a bis-pyridyl amide based ligand (4PNA). The complexes were structurally characterized using SCXRD and the phase purity was confirmed using XRPD. The effect of solvent molecules in dictating the final supramolecular architecture in these SCMs was studied. The copper(II) complex **1** underwent a solvent-mediated crystal-to-crystal transformation to form the thermodynamically stable complex **2**. The solvated crystals of complex **1** were also isolated, which is believed to be the intermediate state in the crystal-to-crystal transformation. The supramolecular complexes and the 1-D coordination polymers of the Zn(II)/Cd(II) benzoates and 4PNA obtained by varying the solvent system revealed the importance of specific solvents in the formation of SCMs. The solid-state interactions of the complexes were studied using Hirshfeld surface analysis and the relative contribution of various non-bonding interactions was quantified. The fluorescence properties of SCMs were analyzed in acetonitrile, where the fluorescence of 4PNA was quenched in copper(II) complexes (**1** and **2**) but the zinc(II)/cadmium(II) SCMs enhanced the emission of 4PNA, which was correlated with the electronic configuration of the respective metal ions. These results indicate the key role of solvent molecules in the formation of SCMs with structural diversities and intriguing properties.

**Supplementary Materials:** The following are available online at <https://www.mdpi.com/2073-8994/13/1/112/s1>, Figure S1:  $^1\text{H}$ -NMR spectra of the supramolecular coordination materials (SCMs) **3–6** in  $\text{DMSO-}d_6$  (400 MHz), Figure S2: Hydrogen bonding interactions (dotted lines) observed in copper(II) SCMs: (a) **1** and (b) **2** (hydrogen atoms except for the donor atoms were omitted for clarity), Figure S3: (a) Molecular structure of **1.S** (hydrogen atoms were omitted for clarity) after excluding the electron densities from the solvent molecules using PLATON/SQUEEZE and (b) a spacefill model showing the solvent accessible voids, Figure S4: Hydrogen bonding interactions (dotted lines) observed in the zinc(II) SCMs: (a) **3** and (b) **4** (phenyl moiety of the benzoate and the hydrogen atoms except for the donor atoms were omitted for clarity), Figure S5: Molecular structure of the coordination polymers (a) **4** and (b) **6** showing the 1-D network, Figure S6: Hydrogen bonding interactions (dotted lines) observed in the cadmium(II) SCMs: (a) **5** and (b) **6** (phenyl moiety of the benzoate and the hydrogen atoms except for the donor atoms were omitted for clarity), Figure S7: Comparison of the X-ray powder diffraction (XRPD) patterns of the simulated and as-synthesized complexes **1** and **1.S**, Figure S8: Comparison of the XRPD patterns of the simulated and as-synthesized complex **3**, Figure S9: Comparison of the XRPD patterns of the simulated and as-synthesized coordination polymer **4**, Figure S10: Comparison of the XRPD patterns of the simulated and as-synthesized complex **5**, Figure S11: Comparison of the XRPD patterns of the simulated and as-synthesized coordination polymer **6**, Figure S12: Hirshfeld surface analysis plotted on the  $d_{\text{norm}}$  maps of **1.S** (with an unrefined solvent molecule) (a) single molecule and (b) three-molecule aggregation showing the close contacts, Figure S13: The overall two-dimensional fingerprint plots of the SCMs **1–6** and the percentage contributions from the specific non-bonding interactions, Figure S14: Hirshfeld surface analysis of the SCMs **1–6** based on the specific non-bonding interactions, Figure S15: UV-vis absorbance spectra of the metal benzoates, *N*-(4-pyridyl)nicotinamide (4PNA) ligand, and SCMs **1–6** in MeCN at room temperature ( $10^{-4}$  M concentration), Figure S16: Comparison of the fluorescence intensity of the SCMs with respect to the corresponding metal benzoates and 4PNA ligand in MeCN at room temperature ( $\lambda_{\text{ex}} = 295$  nm), Table S1: Crystal data, Table S2: Hydrogen-bonding table.

**Author Contributions:** Conceptualization, K.K.D.; methodology, D.G. and O.R.; software, K.K.D. and D.G.; validation, D.G., O.R. and D.A.T.; formal analysis, K.K.D. and D.G.; investigation, D.G., O.R. and D.A.T.; resources, K.K.D.; data curation, K.K.D.; writing—original draft preparation, K.K.D.; writing—review and editing, D.G.; visualization, K.K.D.; supervision, K.K.D.; project administration, K.K.D.; funding acquisition, K.K.D. All authors have read and agreed to the published version of the manuscript.



**Funding:** This research received no external funding. We thank the Science Institute and the University of Iceland Research Fund for the financial support. D.G. thanks the University of Iceland Research Fund for Doctoral Research. We thank the Rannis Iceland Infrastructure grant (150998–0031) for the single-crystal X-ray diffractometer.

**Acknowledgments:** We thank Friðrik Magnus, University of Iceland, for the X-ray powder diffraction instrument and Sigridur Jonsdottir, University of Iceland, for the NMR and mass spectroscopy.

**Conflicts of Interest:** The authors declare no conflict of interest.

## References

1. Beatty, A.M. Hydrogen bonded networks of coordination complexes. *CrystEngComm* **2001**, *3*, 243–255. [\[CrossRef\]](#)
2. Saalfrank, R.W.; Maid, H.; Scheurer, A. Supramolecular Coordination Chemistry: The Synergistic Effect of Serendipity and Rational Design. *Angew. Chem. Int. Ed.* **2008**, *47*, 8794–8824. [\[CrossRef\]](#) [\[PubMed\]](#)
3. Therrien, B. Combining Coordination and Hydrogen Bonds to Develop Discrete Supramolecular Metalla-Assemblies. *Chemistry* **2020**, *2*, 565–576. [\[CrossRef\]](#)
4. Datta, S.; Saha, M.L.; Stang, P.J. Hierarchical Assemblies of Supramolecular Coordination Complexes. *Acc. Chem. Res.* **2018**, *51*, 2047–2063. [\[CrossRef\]](#) [\[PubMed\]](#)
5. Burrows, A.D.; Chan, C.-W.; Chowdhry, M.M.; McGrady, J.E.; Mingos, D.M.P. Multidimensional crystal engineering of bifunctional metal complexes containing complementary triple hydrogen bonds. *Chem. Soc. Rev.* **1995**, *24*, 329–339. [\[CrossRef\]](#)
6. Philp, D.; Stoddart, J.F. Self-Assembly in Natural and Unnatural Systems. *Angew. Chem. Int. Ed.* **1996**, *35*, 1154–1196. [\[CrossRef\]](#)
7. Pöthig, A.; Casini, A. Recent Developments of Supramolecular Metal-based Structures for Applications in Cancer Therapy and Imaging. *Theranostics* **2019**, *9*, 3150–3169. [\[CrossRef\]](#)
8. Ghosh, T.; Maiya, B.G.; Samanta, A.; Shukla, A.D.; Jose, D.A.; Kumar, D.K.; Das, A. Mixed-ligand complexes of ruthenium(II) containing new photoactive or electroactive ligands: Synthesis, spectral characterization and DNA interactions. *J. Biol. Inorg. Chem.* **2005**, *10*, 496. [\[CrossRef\]](#)
9. Adriaenssens, L.; Ballester, P. Hydrogen bonded supramolecular capsules with functionalized interiors: The controlled orientation of included guests. *Chem. Soc. Rev.* **2013**, *42*, 3261–3277. [\[CrossRef\]](#) [\[PubMed\]](#)
10. Amouri, H.; Desmarests, C.; Moussa, J. Confined Nanospaces in Metallogages: Guest Molecules, Weakly Encapsulated Anions, and Catalyst Sequestration. *Chem. Rev.* **2012**, *112*, 2015–2041. [\[CrossRef\]](#) [\[PubMed\]](#)
11. Fang, Y.; Powell, J.A.; Li, E.; Wang, Q.; Perry, Z.; Kirchon, A.; Yang, X.; Xiao, Z.; Zhu, C.; Zhang, L.; et al. Catalytic reactions within the cavity of coordination cages. *Chem. Soc. Rev.* **2019**, *48*, 4707–4730. [\[CrossRef\]](#)
12. Natale, D.; Mareque-Rivas, J.C. The combination of transition metal ions and hydrogen-bonding interactions. *Chem. Commun.* **2008**, *4*, 425–437. [\[CrossRef\]](#) [\[PubMed\]](#)
13. Cook, T.R.; Zheng, Y.-R.; Stang, P.J. Metal–Organic Frameworks and Self-Assembled Supramolecular Coordination Complexes: Comparing and Contrasting the Design, Synthesis, and Functionality of Metal–Organic Materials. *Chem. Rev.* **2013**, *113*, 734–777. [\[CrossRef\]](#) [\[PubMed\]](#)
14. Krische, M.J.; Lehn, J.-M. The Utilization of Persistent H-Bonding Motifs in the Self-Assembly of Supramolecular Architectures. In *Molecular Self-Assembly Organic Versus Inorganic Approaches*; Fuiita, M., Ed.; Springer: Berlin/Heidelberg, Germany, 2000; pp. 3–29.
15. Chen, L.; Berry, S.N.; Wu, X.; Howe, E.N.W.; Gale, P.A. Advances in Anion Receptor Chemistry. *Chem* **2020**, *6*, 61–141. [\[CrossRef\]](#)
16. Piepenbrock, M.-O.M.; Lloyd, G.O.; Clarke, N.; Steed, J.W. Metal- and Anion-Binding Supramolecular Gels. *Chem. Rev.* **2010**, *110*, 1960–2004. [\[CrossRef\]](#)
17. Byrne, P.; Turner, D.R.; Lloyd, G.O.; Clarke, N.; Steed, J.W. Gradual Transition from NH-Pyridyl Hydrogen Bonding to the NH-O Tape Synthon in Pyridyl Ureas. *Cryst. Growth Des.* **2008**, *8*, 3335–3344. [\[CrossRef\]](#)
18. Kumar, D.K.; Jose, D.A.; Dastidar, P.; Das, A. Nonpolymeric Hydrogelator Derived from N-(4-Pyridyl)isonicotinamide. *Langmuir* **2004**, *20*, 10413–10418. [\[CrossRef\]](#)
19. Aakeröy, C.B. Supramolecular assembly of low-dimensional silver(I) architectures via amide–amide hydrogen bonds. *Chem. Commun.* **1998**, *10*, 1067–1068. [\[CrossRef\]](#)
20. Qin, Z.; Jennings, M.C.; Puddephatt, R.J. Stacked molecular triangles: Self-assembly using coordination chemistry and hydrogen bonding. *Chem. Commun.* **2001**, 2676–2677. [\[CrossRef\]](#)
21. Rajput, A.; Mukherjee, R. Coordination chemistry with pyridine/pyrazine amide ligands. Some noteworthy results. *Coord. Chem. Rev.* **2013**, *257*, 350–368. [\[CrossRef\]](#)
22. Dastidar, P.; Roy, R.; Parveen, R.; Ganguly, S.; Majumder, J.; Paul, M. Chapter 2 Designing Soft Supramolecular Materials Using Intermolecular Interactions. In *Functional Supramolecular Materials: From Surfaces to MOFs*; Banerjee, R., Ed.; The Royal Society of Chemistry: London, UK, 2017; pp. 37–74.
23. Mishra, A.; Gupta, R. Supramolecular architectures with pyridine-amide based ligands: Discrete molecular assemblies and their applications. *Dalton Trans.* **2014**, *43*, 7668–7682. [\[CrossRef\]](#) [\[PubMed\]](#)
24. Ay, B.; Şahin, O.; Saygideğer Demir, B.; Saygideğer, Y.; López-de-Luzuriaga, J.M.; Mahmoudi, G.; Safin, D.A. Antitumor effects of novel nickel–hydrazone complexes in lung cancer cells. *New J. Chem.* **2020**, *44*, 9064–9072. [\[CrossRef\]](#)

25. Belda, O.; Moberg, C. Bispyridylamides—Coordination chemistry and applications in catalytic reactions. *Coord. Chem. Rev.* **2005**, *249*, 727–740. [CrossRef]
26. Ghosh, D.; Deepa; Damodaran, K.K. Metal complexation induced supramolecular gels for the detection of cyanide in water. *Supramol. Chem.* **2020**, *32*, 276–286. [CrossRef]
27. Lincheneau, C.; Leonard, J.P.; McCabe, T.; Gunnlaugsson, T. Lanthanide directed self-assembly formations of Tb(iii) and Eu(iii) luminescent complexes from tryptophan based pyridyl amide ligands. *Chem. Commun.* **2011**, *47*, 7119–7121. [CrossRef]
28. Liu, G.-C.; Lu, X.; Li, X.-W.; Wang, X.-L.; Xu, N.; Li, Y.; Lin, H.-Y.; Chen, Y.-Q. Metal/Carboxylate-Induced Versatile Structures of Nine 0D→3D Complexes with Different Fluorescent and Electrochemical Behaviors. *ACS Omega* **2019**, *4*, 17366–17378. [CrossRef]
29. Wang, Y.; Huang, Y.-Q.; Liu, G.-X.; Okamura, T.-a.; Doi, M.; Sheng, Y.-W.; Sun, W.-Y.; Ueyama, N. New Metal-Organic Frameworks with Large Cavities: Selective Sorption and Desorption of Solvent Molecules. *Chem. Eur. J.* **2007**, *13*, 7523–7531. [CrossRef]
30. Adarsh, N.N.; Chakraborty, A.; Tarrés, M.; Dey, S.; Novio, F.; Chattopadhyay, B.; Ribas, X.; Ruiz-Molina, D. Ligand and solvent effects in the formation and self-assembly of a metallosupramolecular cage. *New J. Chem.* **2017**, *41*, 1179–1185. [CrossRef]
31. Kumar, D.K.; Das, A.; Dastidar, P. Supramolecular structural diversities in the metal–organic frameworks derived from pyridylamide ligands: Studying the effects of ligating topologies, hydrogen bonding backbone of the ligands and counter anions. *CrystEngComm* **2007**, *9*, 548–555. [CrossRef]
32. Adarsh, N.N.; Kumar, D.K.; Dastidar, P. Metal–organic frameworks derived from bis-pyridyl-bis-amide ligands: Effect of positional isomerism of the ligands, hydrogen bonding backbone, counter anions on the supramolecular structures and selective crystallization of the sulfate anion. *CrystEngComm* **2009**, *11*, 796–802. [CrossRef]
33. Wang, X.; Liu, Y.; Lin, H.; Xu, N.; Liu, G.; Wang, X.; Chang, Z.; Li, J. A novel cadmium metal–organic framework-based multiresponsive fluorescent sensor demonstrating outstanding sensitivities and selectivities for detecting NB, Fe<sup>3+</sup> ions and Cr<sub>2</sub>O<sub>7</sub><sup>2−</sup> anions. *CrystEngComm* **2020**, *22*, 6626–6631. [CrossRef]
34. Kumar, D.K.; Das, A.; Dastidar, P. Conformation dependent network structures in the coordination polymers derived from pyridylisonicotinamides, carboxylates and Co(ii): Entrapment of (H<sub>2</sub>O)<sub>14</sub> water cluster of an unprecedented topology. *CrystEngComm* **2007**, *9*, 895–901. [CrossRef]
35. Ghosh, D.; Lebedyť, I.; Yufit, D.S.; Damodaran, K.K.; Steed, J.W. Selective gelation of N-(4-pyridyl)nicotinamide by copper(ii) salts. *CrystEngComm* **2015**, *17*, 8130–8138. [CrossRef]
36. Xu, N.; Zhang, J.W.; Wang, X.L.; Liu, G.C.; Li, T.J. Solvent-induced Mn(II)/Zn(II)/Co(II) organopolymolybdate compounds constructed by bis-pyridyl-bis-amide ligands through the Mo–N bond: Synthesis, structures and properties. *Dalton Trans.* **2016**, *45*, 760–767. [CrossRef]
37. Mahat Chhetri, P.; Yang, X.-K.; Chen, J.-D. Mercury halide coordination polymers exhibiting reversible structural transformation. *CrystEngComm* **2018**, *20*, 2126–2134. [CrossRef]
38. Tzeng, B.-C.; Hung, Y.-C.; Lee, G.-H. Anion- and Solvent-Induced Assembly and Reversible Structural Transformation of d10-Metal Coordination Architectures Containing N-(4-(4-Aminophenoxy)phenyl)isonicotinamide. *Chem. Eur. J.* **2016**, *22*, 1522–1530. [CrossRef]
39. Huang, C.; Wang, Y.; Wei, C.; Li, N.; Ji, F.; Wu, J.; Hou, H. Cation-exchange-induced single-crystal-to-single-crystal transformations of a nanoporous coordination complex. *Inorg. Chem. Commun.* **2013**, *32*, 68–73. [CrossRef]
40. Gong, Z.-L.; Zhong, Y.-W. H<sub>2</sub>PO<sub>4</sub><sup>−</sup> and Solvent-Induced Polymorphism of an Amide-Functionalized [Pt(N<sup>ˆ</sup>C<sup>ˆ</sup>N)Cl] Complex. *Inorg. Chem.* **2016**, *55*, 10143–10151. [CrossRef]
41. Zhang, L.; Dang, L.; Luo, F.; Feng, X. Solvent-controlled assembly of crystal structures: From centrosymmetric structure to noncentrosymmetric structure. *J. Mol. Struct.* **2016**, *1106*, 114–120. [CrossRef]
42. Sheldrick, G.M. Crystal structure refinement with SHELXL. *Acta Crystallogr. Sect. C Struct. Chem.* **2015**, *71*, 3–8. [CrossRef]
43. Spek, A. PLATON SQUEEZE: A tool for the calculation of the disordered solvent contribution to the calculated structure factors. *Acta Crystallogr. Sect. C* **2015**, *71*, 9–18. [CrossRef] [PubMed]
44. Turner, M.; McKinnon, J.; Wolff, S.; Grimwood, D.; Spackman, P.; Jayatilaka, D.; Spackman, M. *CrystalExplorer17*; The University of Western Australia: Perth, WA, Australia, 2017. Available online: <https://crystalexplorer.scb.uwa.edu.au/> (accessed on 25 December 2020).
45. Tan, S.L.; Jotani, M.M.; Tiekink, E.R.T. Utilizing Hirshfeld surface calculations, non-covalent interaction (NCI) plots and the calculation of interaction energies in the analysis of molecular packing. *Acta Crystallogr. Sect. E* **2019**, *75*, 308–318. [CrossRef] [PubMed]
46. Aggarwal, H.; Bhatt, P.M.; Bezuidenhout, C.X.; Barbour, L.J. Direct evidence for single-crystal to single-crystal switching of degree of interpenetration in a metal-organic framework. *J. Am. Chem. Soc.* **2014**, *136*, 3776–3779. [CrossRef] [PubMed]
47. Zhang, J.-P.; Liao, P.-Q.; Zhou, H.-L.; Lin, R.-B.; Chen, X.-M. Single-crystal X-ray diffraction studies on structural transformations of porous coordination polymers. *Chem. Soc. Rev.* **2014**, *43*, 5789–5814. [CrossRef] [PubMed]
48. Kole, G.K.; Vittal, J.J. Solid-state reactivity and structural transformations involving coordination polymers. *Chem. Soc. Rev.* **2013**, *42*, 1755–1775. [CrossRef] [PubMed]
49. He, Y.-C.; Yang, J.; Liu, Y.-Y.; Ma, J.-F. Series of Solvent-Induced Single-Crystal to Single-Crystal Transformations with Different Sizes of Solvent Molecules. *Inorg. Chem.* **2014**, *53*, 7527–7533. [CrossRef]
50. Chaudhary, A.; Mohammad, A.; Mobin, S.M. Recent Advances in Single-Crystal-to-Single-Crystal Transformation at the Discrete Molecular Level. *Cryst. Growth Des.* **2017**, *17*, 2893–2910. [CrossRef]

51. Braga, D.; Brammer, L.; Champness, N.R. New trends in crystal engineering. *CrystEngComm* **2005**, *7*, 1–19. [[CrossRef](#)]
52. Liu, Z.; He, W.; Guo, Z. Metal coordination in photoluminescent sensing. *Chem. Soc. Rev.* **2013**, *42*, 1568–1600. [[CrossRef](#)]
53. Barbieri, A.; Accorsi, G.; Armaroli, N. Luminescent complexes beyond the platinum group: The d10 avenue. *Chem. Commun.* **2008**, *19*, 2185–2193. [[CrossRef](#)]
54. Zheng, S.-L.; Chen, X.-M. Recent Advances in Luminescent Monomeric, Multinuclear, and Polymeric Zn(II) and Cd(II) Coordination Complexes. *Aust. J. Chem.* **2004**, *57*, 703–712. [[CrossRef](#)]
55. Erxleben, A. Structures and properties of Zn(II) coordination polymers. *Coord. Chem. Rev.* **2003**, *246*, 203–228. [[CrossRef](#)]
56. Wang, S. Luminescence and electroluminescence of Al(III), B(III), Be(II) and Zn(II) complexes with nitrogen donors. *Coord. Chem. Rev.* **2001**, *215*, 79–98. [[CrossRef](#)]
57. Jiang, P.; Guo, Z. Fluorescent detection of zinc in biological systems: Recent development on the design of chemosensors and biosensors. *Coord. Chem. Rev.* **2004**, *248*, 205–229. [[CrossRef](#)]
58. Evans, R.C.; Douglas, P.; Winscom, C.J. Coordination complexes exhibiting room-temperature phosphorescence: Evaluation of their suitability as triplet emitters in organic light emitting diodes. *Coord. Chem. Rev.* **2006**, *250*, 2093–2126. [[CrossRef](#)]
59. De Almeida, A.; Bonsignore, R. Fluorescent metal-based complexes as cancer probes. *Bioorg. Med. Chem. Lett.* **2020**, *30*, 127219. [[CrossRef](#)]
60. Jeong, Y.; Yoon, J. Recent progress on fluorescent chemosensors for metal ions. *Inorg. Chim. Acta* **2012**, *381*, 2–14. [[CrossRef](#)]
61. Cheng, W.; Xie, Y.; Yang, Z.; Sun, Y.; Zhang, M.-Z.; Ding, Y.; Zhang, W. General Strategy for in Situ Generation of a Coumarin-Cu<sup>2+</sup> Complex for Fluorescent Water Sensing. *Anal. Chem.* **2019**, *91*, 5817–5823. [[CrossRef](#)]
62. Yang, X.-L.; Xie, M.-H.; Zou, C.; Wu, C.-D. Syntheses, crystal structures and optical properties of six homochiral coordination networks based on phenyl acid-amino acids. *CrystEngComm* **2011**, *13*, 6422–6430. [[CrossRef](#)]
63. Wang, X.W.; Chen, J.-Z.; Liu, J.-H. Photoluminescent Zn(II) Metal–Organic Frameworks Built from Tetrazole Ligand: 2D Four-Connected Regular Honeycomb (4363)-net. *Cryst. Growth Des.* **2007**, *7*, 1227–1229. [[CrossRef](#)]